Journal of Sol-Gel Science and Technology
https://doi.org/10.1007/s10971-022-05951-5

ORIGINAL PAPER: NANO-STRUCTURED MATERIALS (PARTICLES, FIBRES, COLLOIDS, COMPOSITES, ETC.)

Effect of embedding aluminium and yttrium on the magneto-optic properties of lanthanum spinel ferrite nanoparticles synthesised for photocatalytic degradation of methyl red

Subiya K. Kazi[1] · Radhakrishnan M. Tigote[1] · Vandana A. Gaikwad[1] · Dhanraj P. Kamble[2] · Pravin S. Bhale[3] · Sadanand N. Shringare[4] · Pramod G. Musrif[5] · Shaukatali N. Inamdar[6]

Received: 8 August 2022 / Accepted: 20 September 2022

Abstract

The sol-gel approach was used to synthesise lanthanum and aluminium doped yttrium ferrite nanoparticles. The absorption peak is observed at ~265 nm corresponds to band gap of 2.9–3.1 eV. X-ray diffraction (XRD), field emission scanning electron microscopy (FE-SEM) and High-Resolution Transmission Electron Microscopy (HR – TEM) were used to analyse the structural and microstructural properties of the product. The particle size calculated to be 60–110 nm from the HR-TEM analysis. The vibrating sample magnetometer (VSM) showed high magnetisation with reversible loop and increased surface-induced magnetisation, the presence of all elements were confirmed using energy Dispersive X-Ray Spectroscopy (EDS). From BET analysis, the surface area, pore volume and pore diameter are 2.688 $m^2 g^{-1}$, 5.178 $cm^3 g^{-1}$ and 7.704 nm respectively, the isotherm represents type (V), with an H_3 hysteresis loop. The obtained product, $La_{1-X}Al_XY_YFe_{2-Y}O_4$, showed good photo-catalytic activity when employed for the photo-catalytic degradation of methyl red dye within 210 min.

Graphical abstract

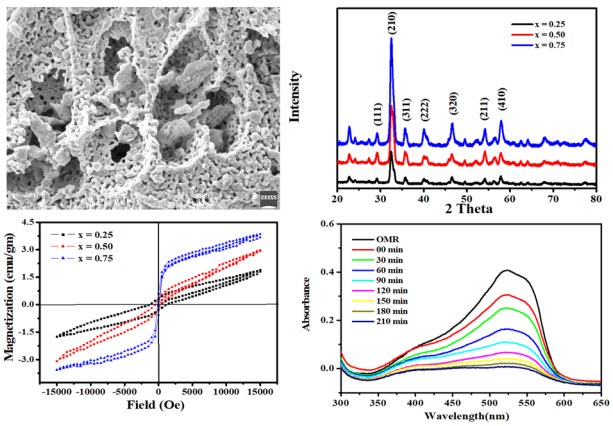

✉ Radhakrishnan M. Tigote
rmtigote.chemobad@bamu.ac.in

[1] Department of Chemistry, Dr. Babasaheb Ambedkar Marathwada University, Subcampus Osmanabad, Maharashtra 413501, India

[2] Department of Chemistry, S.B.E.S. College of Science, Aurangabad, Maharashtra 431001, India

[3] Department of Chemistry, Yashwant Chavan Mahavidyalaya, Tuljapur, Osmanabad, Maharashtra 413601, India

[4] School of Chemical Sciences, Punyashlok Ahilyadevi Holkar Solapur University, Solapur, Maharashtra 413255, India

[5] Department of Engineering Sciences, AISSMS, Institute of Information Technology, Pune, Maharashtra 411001, India

[6] Department of Pharmaceutical Chemistry, College of Health Sciences, University of KwaZulu-Natal (Westville), Durban 4000, South Africa

Published online: 08 October 2022

Keywords Sol–gel approach · Magnetic effect · Optical characteristics · Microstructural property · Photo-catalytic degradation

Highlights

- The lattice constant increases in the concentration of x, indicating the cubic spinel structure.
- In $La_{1-X}Al_XY_YFe_{2-Y}O_4$ Bohr magneton, anisotropy and coercivity increases with increase in the concentration of x.
- Ms, Mr increases with concentration of Aluminium and Yttrium substitution, confirming the B-site occupancy of Lanthanum ion.
- Catalyst for the successful photocatalytic degradation of methyl red dye within 210 min.

1 Introduction

Nanomaterials played a significant role in research over the last few decades due to their better qualities than their bulk counterparts [1–3]. After that, on ferrite and lanthanum orthoferrites are promising nanomaterial for use as nonstoichiometric anionic deficient perovskite electrodes. The lanthanum yttrium aluminium ferrite are reported exhibiting significant increase in magnetic and electrical power production in the temperature range of 650–900 °C [4–10]. The dopant could also boost intrinsic activity at each electrochemically active site [11]. Lanthanum ferrite is a type of mixed electronic ionic conductor utilised in solid oxide fuel cells as a cathode. The many metals doped on lanthanum ferrite have a wide range of applications [12] and distorted perovskite-type ferrite is lanthanum orthoferrites or lanthanum ferrites are observed in gas sensing properties as excellent. Due to its unusual opto-electronic characteristics and narrow band gap, it has also been discovered to be a photocatalytically active catalyst [4–10] with ceramic technology ideas [13–15].

The spinel structure of the concentration of Lanthanum is closely related to the concentration of point defects in transition metal oxides, which is known as defect chemistry [16–22]. Doping with yttrium ions is expected to provide refractoriness with a coefficient of thermal expansion well matched to the yttria-stabilised zirconia. Doped lanthanum ferrite is known to have high mixed electronic and oxygen ion conductivities, and doping with yttrium ions is expected to provide refractoriness with a coefficient of thermal expansion well matched to the yttria-stabilised zirconia [23]. The conversion of mechanical to electrical energy is a major application of storing energy in a static magnetic field with general formula for magnetic spinel is MFe_2O_4 [24–26]. It is also fascinating to study the structural, optical, electrical, magnetic, and other features from a magnetic perspective. Once ferromagnetic (Fe^{3+}) atoms are replaced by paramagnetic ($A1^{3+}$) atoms in this type of material, partial and full substitution of ferromagnetic (Fe^{3+}) atoms by paramagnetic ($A1^{3+}$) [27, 28]. Low-cost alternative oxides with layered structures and previous oxide/redox reaction capabilities, as well as perovskite p-type functional oxides are thought to be variables for use as electrodes in super capacitor designs [29–31].

In all perovskite cells, the reported copper-doped lanthanum ferrites were examined in both oxidising and reducing circumstances [32]. The super-capacitor has gained a lot of interest in recent years as a new type of energy storage device due to its extended cycle life, high efficiency, high power density, and environmentally benign qualities. Because of their pseudo-capacitance change storing mechanism, transition metal oxides have shown to be excellent electrode materials for super capacitors. The increased surface-to-volume ratio of ferrites leads to enhanced ionic/atomic reactivity on the surface of particles compared to those present within the particles, resulting in dramatic fluctuations in electrical and magnetic properties. Recently, Because of their vast range of technical applications in domains such as hyperthermia, cell biology, and molecular imaging, ferrites have been intensively explored [33–35]. Because spinel ferrites have tetrahedral—A and octahedral—B sites in their crystal structure, the cation distribution among these sites has a significant impact on their physical characteristics. The octahedral sites are difficult to disperse into the lattice to process the formation of the ferrite particles due to the smallness of the tetrahedral sites. Experiments are highly useful in determining the exact number of rare earth ions in the crystal lattice and their effects on various physical properties [36].

The synthesis of pure ferrites is a hard process. The reason for this is that cation diffusion into the lattice occurs in numerous stages, each with its own set of challenges in terms of valence, imbalance, and defective structure creation. Single crystalline ferrites perform better than polycrystalline ferrites in microwave applications [37]. Soft ferrites have an FCC closed-packed spinel crystal structure and include both divalent and trivalent cations [38]. Because of their good stability at high temperatures under reducing conditions and high oxygen flux rates, doped lanthanum ferrite materials have been proven to be ideal as in oxygen transport membranes in syngas reactors [39]. The behaviour of nanoparticles is influenced by a variety of characteristics in the system, including grain and grain border structure, particle size distribution, and inter-particle

interactions [40]. In their study of perovskite, particle is dictated by the yttria stabilised zirconia [41]. Some of the scientists note that the material has some interesting properties for a variety of applications, including redox stability, strong electronic conductivity, and good electrocatalytic activity [42]. In the observation, the doping rare earth and transition elements into doped mixed ferrites results in magnetisation by dominating the Spinal spin Structure [43]. In such all cases, chemical co precipitation, glass crystallisation, organic resin method, sol–gel method, and ceramic process have all been used to make lanthanum, aluminium, and yttrium ferrites [44] and their applications towards Hyperthermia, cell biology, molecular imaging etc. [45–47] and also photo-catalytically active for degradation of various drugs and dyes [48, 49].

So, said adopted synthesised material is used to control the size, shape, compositions, multifunctionalities with their structural properties of micro- materials but the advanced studies are help to understand the properties of nanoscale magnetic materials. Thus, in the present works, herein report the new synthesis of lanthanum doping spinel ferrite composite Nanomaterial by using sol–gel method and shown the effect of contents of yttrium and aluminium ion on their magnetic properties performed. The morphology and structural characterisation of the produced Nanocomposites were characterised by X-ray diffraction, energy dispersive spectroscopy, high resolution-transmission electron microscopy and vibrating sample magnetometer. The synthesized $La_{1-X}Al_XY_YFe_{2-Y}O_4$ shown the photocatalytic activity into degradation of methyl red dye is to be found successfully within 210 min.

2 Material and methods

The required materials for the preparation of $La_{1-X}Al_XY_YFe_{2-Y}O_4$ are purchased from HI media and used without purification. Lanthanum nitrate La $(NO_3)_3{\cdot}6H_2O$, Aluminium nitrate Al $(NO_3)_3{\cdot}9H_2O$, Yttrium nitrate $Y(NO_3)_3{\cdot}6H_2O$, and ferric nitrate Fe $(NO_3)_3{\cdot}9H_2O$ were used as sources of La, A1, Y and Fe, with citric acid as a complexing agent. All of the chemicals are of A.R. quality.

2.1 Methods

For the new synthesis of $La_{1-X}Al_XY_YFe_{2-Y}O_4 (x = 0.25, 0.50, 0.75)$, the nitrates of lanthanum, aluminium, yttrium and iron was taken in 20 ml distil water. To this beaker after solubility of all nitrate's, citric acid (1:4) portion was added and reaction continued, stirring at maintained at temperature 80 °C for 2 h and the solution get converted into gel. Again, Gel was completely dried within next 3 h to afford fine powder of $La_{1-X}Al_XY_YFe_{2-Y}O_4$. This raw powder was calcinated at 900 °C for 2 h, then the sample was ready for all characterisation.

Table 1 Optical band gap of $La_{1-X}Al_XY_YFe_{2-Y}O_4$ series

Sr.No.	% Doping of			Optical Band Gap
	La	Al	Y	
1	0.75	0.25	0.25	3.1
2	0.50	0.50	0.50	3.0
3	0.25	0.75	0.75	2.9

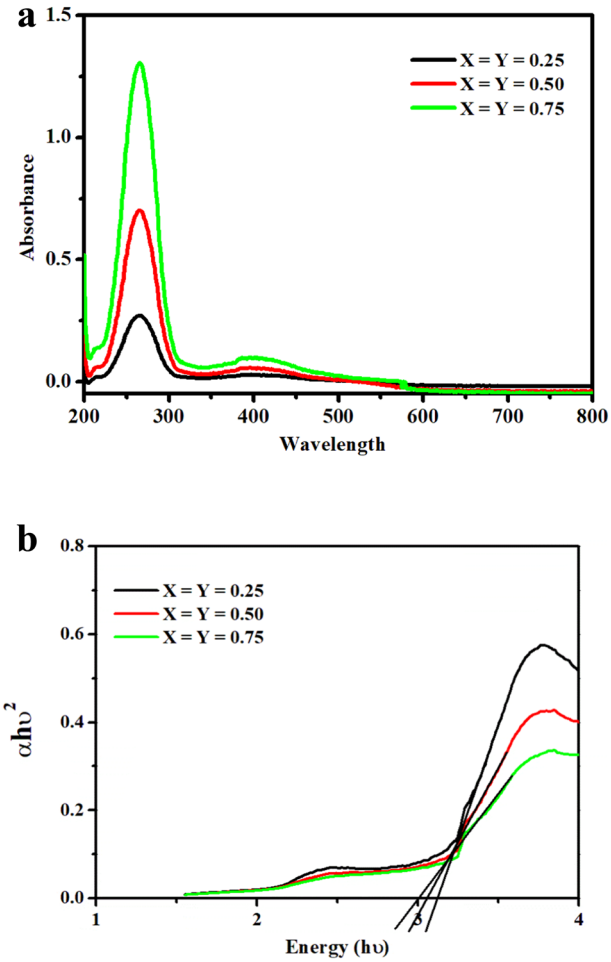

Fig. 1 **a** UV–visible spectra of $La_{1-X}Al_XY_YFe_{2-Y}O_4$ series. **b** TAUC Plot of $La_{1-X}Al_XY_YFe_{2-Y}O_4$ series

3 Result and discussion

A series of $La_{1-X}Al_XY_YFe_{2-Y}O_4$ $(x = 0.25, 0.50, 0.75)$ has been successfully synthesised by employing the sol–gel technique. A UV–visible spectrophotometer is used to determine the absorption peak and band gap of a series. XRD was used to determine particle size, crystal structure, X-ray density, octahedral and tetrahedral sites, and interplanar distance. Field emission scanning electron microscopy was used to determine structural morphology (FE-SEM). The elemental analysis of a series, which is provided by energy dispersive spectroscopy (EDS). Vibrating sample magnetometer was used to investigate

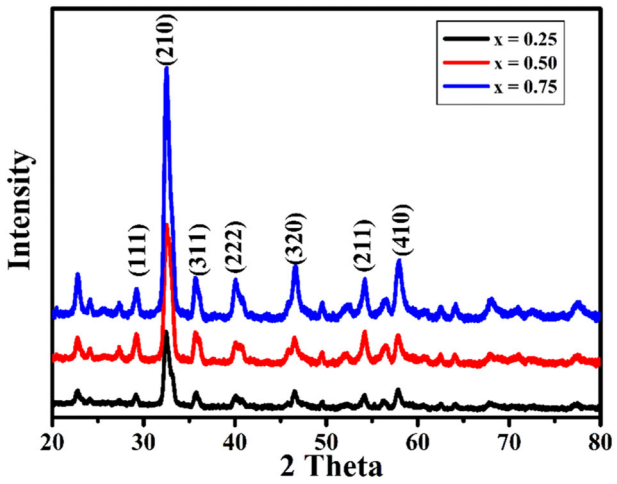

Fig. 2 XRD spectrum of $La_{1-X}Al_XY_YFe_{2-Y}O_4$ series

the magnetic characteristics (VSM), crystalline nature and ensure particle size by HR- TEM technique. The photocatalytic application towards the degradation of methyl red dye within 210 min.

3.1 Optical study

For the analysis of optical properties of a $La_{1-X}Al_XY_{Y-}Fe_{2-Y}O_4(x = 0.25,\ 0.50,\ 0.75)$ the UV Visible spectrophotometer is used. In the experimental result, all samples were soluble in 0.1 M HCl solution for analysing the maximum absorption peaks at ~265 nm. The band gap of all samples ranges from 2.9 eV to 3.1 eV as shown in Table 1. The conforming band gap decreases as the concentration of Aluminium and Yttrium increases with decrease in concentration of Lanthanum. The UV–Visible spectrum and band gap spectrum is shown in Fig. 1a, b.

The band gap calculated by Tauc's plot relationship is expressed as follows:

$$(\alpha h\upsilon)^{1\backslash n} = C\left(h\upsilon - E_g\right) \tag{1}$$

where, α = the absorption coefficient,

ν = frequency ($\nu = c/\lambda$, h is Planck's constant, λ = wavelength, c = speed of light),

$n = 2$ for direct optical band gap, respectively

C = proportionality constant and

E_g = band gap

3.2 X-ray diffraction (XRD)

The XRD pattern shows the sharp intense peaks of a series of $La_{1-x}Al_XY_YFe_{2-Y}O_4$ ($x = 0.25, 0.50, 0.75$) nanoparticles, which confirms the FCC structure. The peaks indicate planes (111), (210), (311), (222), (320), (211), (410) as shown in Fig. 2. The particle size was calculated by using Debye–Scherrer Equation as,

$$D = \frac{0.9\lambda}{\beta\, COS\,\theta} \tag{2}$$

where $\lambda = 1.543$ Å, β = full width of half maxima. The inter planner distance d was calculated by using formula $d = \lambda/2\mathrm{Sin}\theta$, the lattice parameter a is given as,

$$a = d\sqrt{h^2 + k^2 + l^2} \tag{3}$$

the volume is given by,

$$V = a^3 \tag{4}$$

the X-ray density of the series was calculated by,

$$d_x = \frac{nM}{N_A V} \tag{5}$$

The interplanar distance (d), Lattice constant (a), volume (V) and X-ray density of $La_{1-X}Al_XY_YFe_{2-Y}O_4$ series are mentioned in Table 2. As the concentration of aluminium, yttrium increases with decreasing concentration of lanthanum the inter planar distance and X-ray density goes on decreasing but lattice constant and volume get increased. The crystal structure and average particle size of $La_{1-X}Al_XY_YFe_{2-Y}O_4$ series are mentioned in Table 2. The concentration of aluminium, yttrium increases with decreasing concentration of lanthanum the particle size also decreased from 30 nm to 24 nm. The series shows FCC crystal structure. The hopping length of octahedral and tetrahedral sites is mentioned in Table 3. As the concentration of aluminium, yttrium increases with decreasing concentration of lanthanum, the hopping length of octahedral sites decreases with increase in hopping length of tetrahedral sites shown in Fig. 3 and their variation shown in crystalline size i.e., decreasing order shown in Fig. 4.

3.3 Magnetic measurement by vibrating sample magnetometer (VSM)

In our investigation the magnetic properties of the $La_{1-X}Al_XY_YFe_{2-Y}O_4$ series at a field of 50 kOe produced field-dependent magnetisation including Saturation Magnetisation (M_S), remnant magnetisation (M_r), coercivity (H_C), magnetic moment (B), and anisotropy constant (K_1), it resulted from the M–H loop listed in Table 4. The M_S values rapidly fall with the addition of nonmagnetic La^{3+} due to the creation of non-magnetic spinel structure, as seen in Fig. 5. Additionally, the value of M_S diminishes as the collinear ferromagnetic

Table 2 Inter planar distance (d), Lattice constant (a), Volume (V) and X-ray density (d_x) Average particle size (D) and crystal structure of $La_{1-X}Al_XY_YFe_{2-Y}O_4$ series

Sr. No	X	Y	d	a	V	$d_x * 10^{-23}$	D (nm)	Crystal structure
1	0.25	0.25	0.3174	0.896	7.81	4.2315	30.99	FCC
2	0.50	0.50	0.3250	0.3501	8.82	3.6041	25.37	FCC
3	0.75	0.75	0.3114	1.4540	10.77	1.3452	24.25	FCC

Table 3 Hopping lengths 'L_A' and 'L_B' of $La_{1-X}Al_XY_YFe_{2-Y}O_4$ series

Sr. No.	X	Y	L_A	L_B
1	0.25	0.25	1.6873	0.3770
2	0.50	0.50	0.5845	0.4772
3	0.75	0.75	0.3148	0.5140

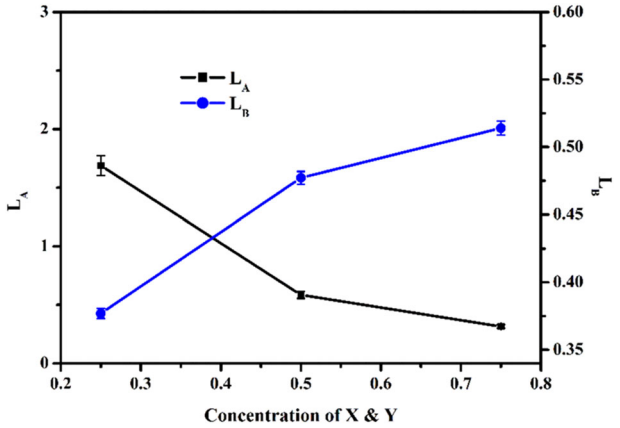

Fig. 3 Hopping length of $La_{1-X}Al_XY_YFe_{2-Y}O_4$ series

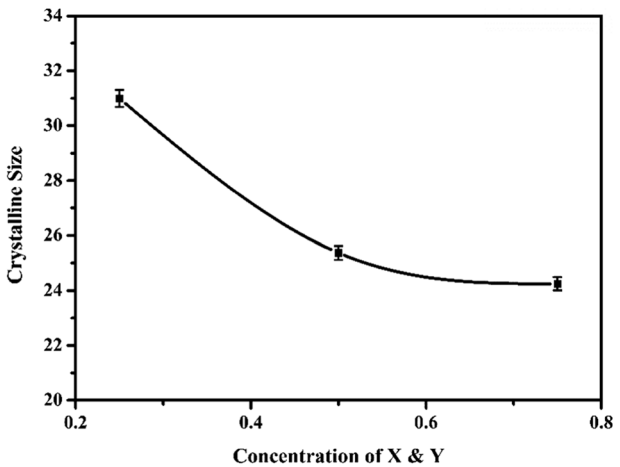

Fig. 4 Variation of crystalline size with concentration of Al & Y for $La_{1-X}Al_XY_YFe_{2-Y}O_4$ series

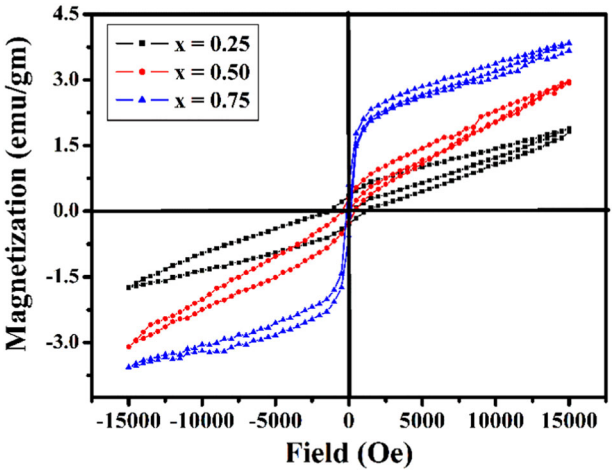

Fig. 5 Magnetic hysteresis loop of $La_{1-X}Al_XY_YFe_{2-Y}O_4$ series

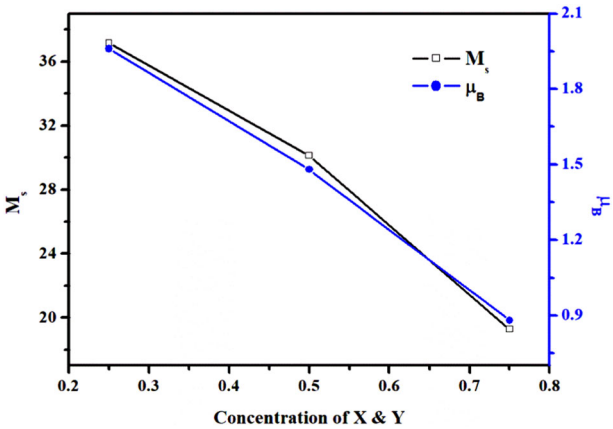

Fig. 6 Variation of saturation magnetisation and coercivity with concentration of Al and Y for $La_{1-X}Al_XY_YFe_{2-Y}O_4$ series

arrangement is converted to non-collinear order. The crystallite size, cation distribution, and exchange energy of the crystals all play a role in this diminishing process. The results improve in surface-to-volume atoms, which form a number of vacancies and interatomic separation, as D is reduced. With the development of trivalent Yttrium ions, these disordered spins over the surface induce magnetism. Furthermore, the cation distribution at the A- and B-sites can explain M_s declining behaviour. In most cases, the iron ion is found in the B site. Some iron ions migrated to the tetrahedral location when Al^{3+}, and Y^{3+} were substituted. Furthermore, replacing the iron ion with the paramagnetic Y^{3+} results in enhanced in net magnetic moment and the coercivity values H_C of ferrites materials are shown in Table 4 and as illustrated in Fig. 6. The experimental μ_B per formula unit was calculated as follows:

$$\mu_B = \frac{M \times M_s}{5585} \tag{6}$$

Table 4 Magnetisation data of $La_{1-X}Al_XY_YFe_{2-Y}O_4$ series

Sr. No.	X and Y concentration	M_S (emu/g)	M_r (emu/g)	M_r/M_S	Coercivity (H_C) (Oe)	μ_B (Bohr magneton)	$K_1 = \frac{M_s H_c}{2} \times 10^4$ (erg/cm^3)
1	0.75	19.27	5.78	0.299	1.11	0.88	10.69
2	0.50	30.13	3.42	0.113	1.57	1.48	23.65
3	0.50	37.16	2.75	0.074	4.49	1.96	83.42

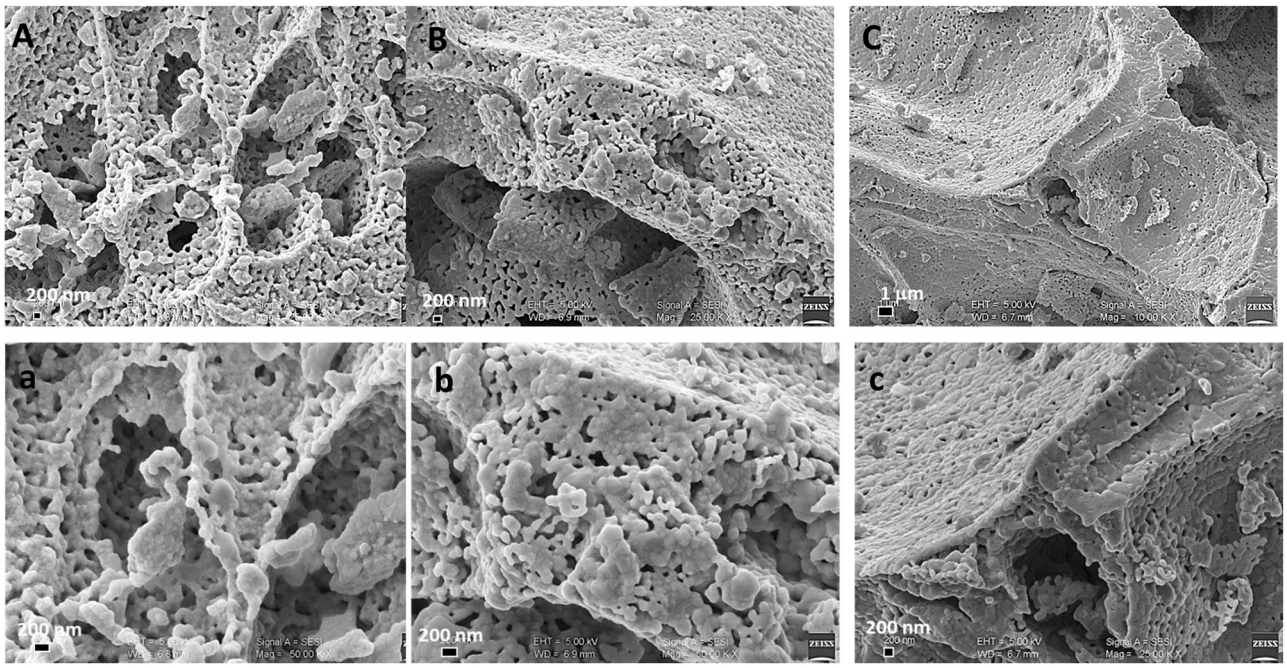

Fig. 7 FE-SEM images of $La_{1-X}Al_XY_YFe_{2-Y}O_4$ Series (**A, a**) 0.25 (**B, b**) 0.50 and (**C, c**) 0.75 conc

3.4 Field emission-scanning electron microscopy (FE-SEM) and energy dispersive spectroscopy (EDS) analysis

Figure 7 shows the effect of trivalent ion substitution in place of iron ion on the surface morphology of $La_{1-X}Al_XY_YFe_{2-Y}O_4$ nano ferrites. The ferrites particles were found to be nearly spherical, with a distinct grain boundary and some agglomeration but their grain behaviour is an important property of ferromagnetic materials. The particle size was computed using the Debye sheerer approach, and it was shown that the particle size decreases with the replacement of Al^{3+}, and Y^{3+}, which exhibits a comparable plane to D_{311} reported in the XRD data. The particle size estimated by FE-SEM is comparable to that determined by XRD, which is a common occurrence. The FE-SEM pictures show highly porous structure of the synthesised nanomaterials.

Figure 8 shows the EDS of $La_{1-X}Al_XY_YFe_{2-Y}O_4$ nanoparticles ($x = 0.25, 0.50, 0.75$). The presence of peaks in the spectra indicates that La, Al, Y, Fe and O are present. There were no impurity peaks in the spectra, indicating that the materials were pure. In Tables 5 and 6, the elemental and atomic proportions of each mixture have been tabulated.

3.5 High resolution-transmission electron microscopy (HR-TEM)

The morphological characteristics have been investigated by high-resolution transmission electron microscopy (HR-TEM) for the samples $La_{1-X}Al_XY_YFe_{2-Y}O_4$ indicated in Fig. 9(A, a), (B, b), and (C, c). Particles with an average size range 80, 120 and 60 nm for the conc. of 0.25, 0.50 and 0.75, respectively. The D_{311} estimated from the XRD data is better presented with the particle size observed in the HR-TEM images. The rings confirm the crystalline nature of the nano ferrites.

3.6 Photocatalytic degradation

By investigating photocatalytic degradation of Methyl red dye, the $La_{1-X}Al_XY_YFe_{2-Y}O_4$ nano-ferrites were considered suitable for catalytic activities. Figure 10a shows the UV–visible absorption spectra of methyl red dye in a

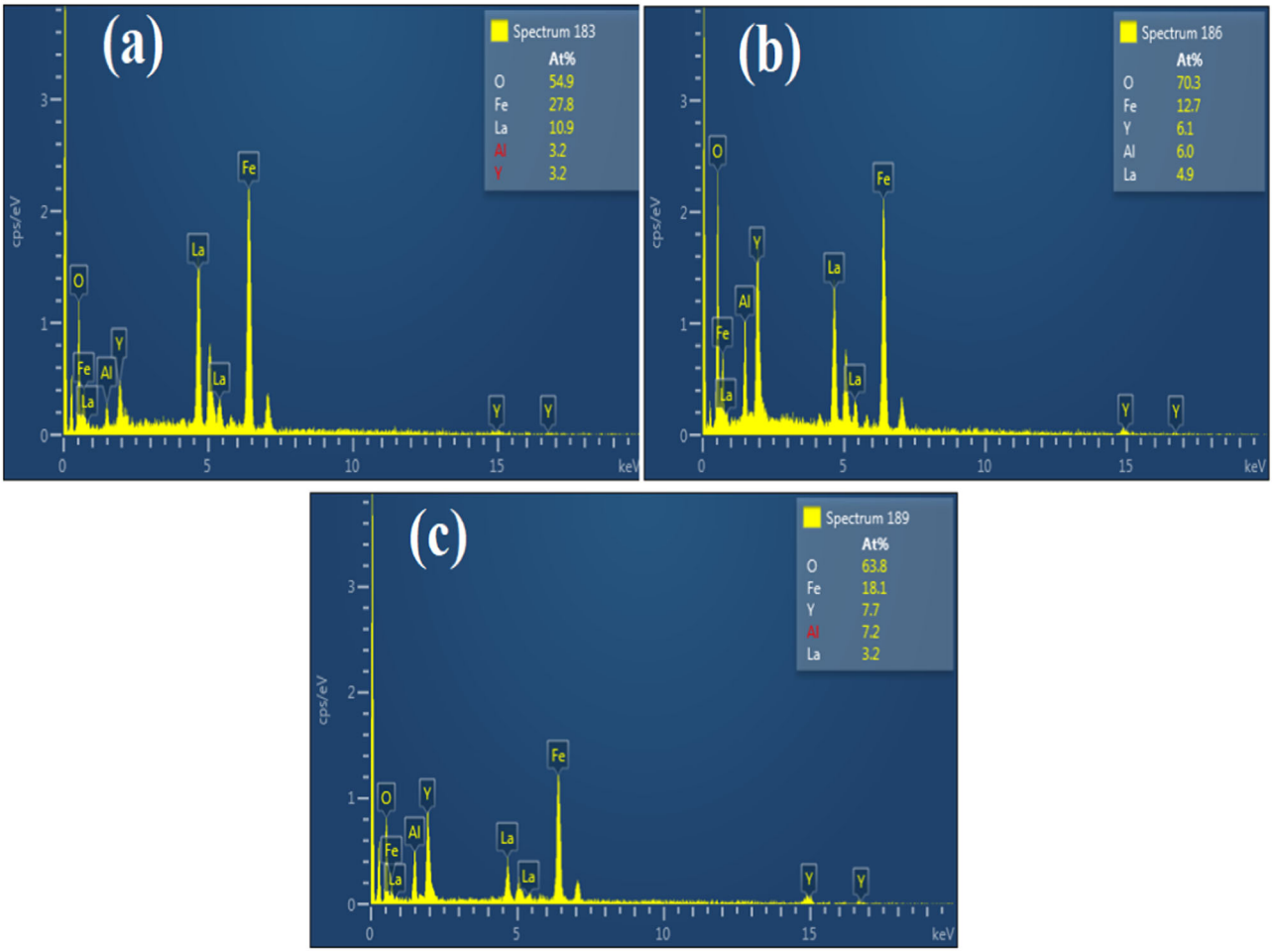

Fig. 8 EDS spectrum of $La_{1-X}Al_XY_YFe_{2-Y}O_4$ Series **a** 0.25, **b** 0.50, **c** 0.75 conc

Table 5 The elements of each sample composition $La_{1-X}Al_XY_YFe_{2-Y}O_4$ nanoparticles analysed by atomic %) obtained by EDS

Sr. No	Composition of nanoparticles	Elemental composition (atomic%)				
		La	Al	Y	Fe	O
1	0.25	45.15	8.77	45.54	18.15	5.19
2	0.50	46.19	8.97	46.59	18.56	6.64
3	0.75	47.28	9.18	47.69	19.00	6.80

Table 6 The elements of each sample composition $La_{1-X}Al_XY_YFe_{2-Y}O_4$ nanoparticles analysed by (wt%) obtained by EDS

Sr. No	Composition of nanoparticles	Elemental composition (wt%)				
		La	Al	Y	Fe	O
1	0.25	44.82	1.69	45.65	7.24	0.59
2	0.50	44.77	1.68	45.55	7.24	0.74
3	0.75	44.77	1.68	45.55	7.23	0.74

suspension of $La_{1-X}Al_XY_YFe_{2-Y}O_4$ nano-ferrites Nano-composite as a function of irradiation time [50, 51]. The characteristic absorption peak of methyl red dye at ~523 nm gradually decreases with time irradiation, as can be observed in the figure. Using $La_{1-X}Al_XY_YFe_{2-Y}O_4$ nano-ferrites composites, substantial degradation of methyl red dye was seen in about 210 min. Figure 10b shows a kinetic graph of the methyl red photodegradation reaction over many catalysts with respect to variable irradiation time. The observation that the concentration of methyl red remained constant in the absence of a photocatalyst in the presence of sunlight implies that the methyl red dye is photochemically very stable. Within 210 min of irradiation, complete methyl red degradation was observed for $X = Y = 0.75$ concentration $La_{1-X}Al_XY_YFe_{2-Y}O_4$ nano-ferrites composites, whereas less degradation was observed for without catalyst, $X = Y = 0.25$ concentration, and $X = Y = 0.50$ concentration $La_{1-X}Al_XY_YFe_{2-Y}O_4$ nano-ferrites composites, respectively. This study indicates that the amount of $La_{1-X}Al_XY_YFe_{2-Y}O_4$ nano-ferrites in the composite is substantially correlated with the photocatalytic degradation process. Furthermore, $La_{1-X}Al_XY_YFe_{2-Y}O_4$ nano-ferrites catalyst has a stronger

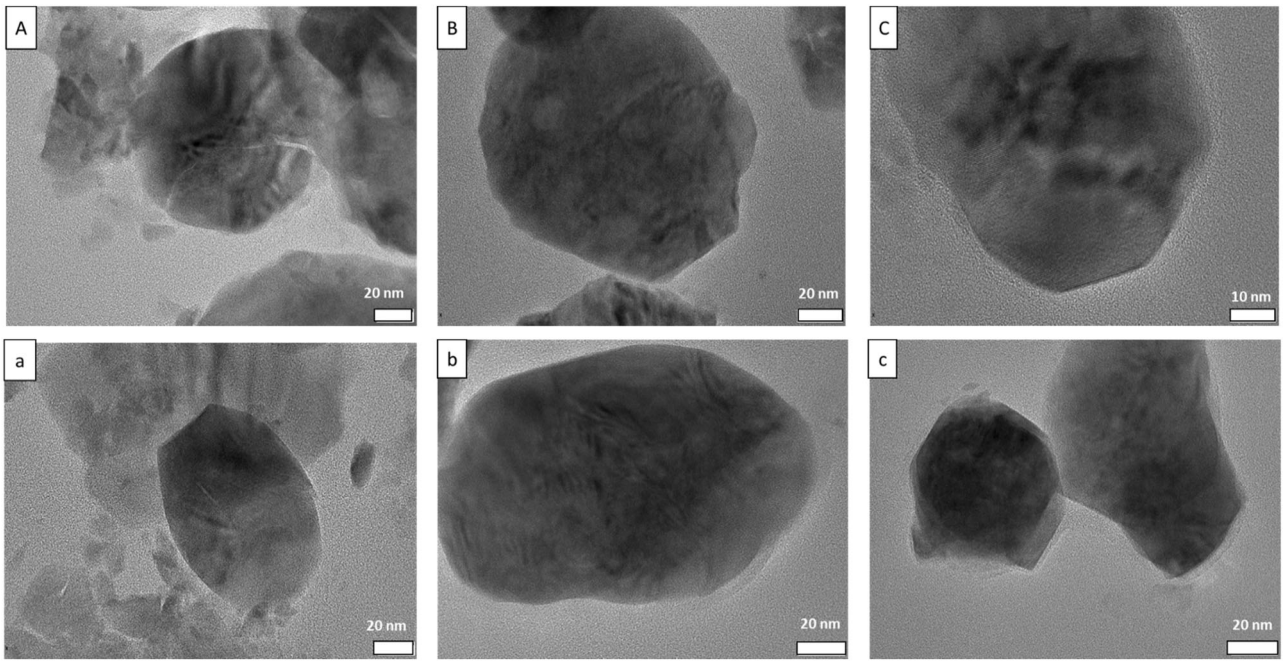

Fig. 9 HR-TEM images of $La_{1-X}Al_XY_YFe_{2-x}O_4$ Series (**A**, **a**) 0.25 (**B**, **b**) 0.50 and (**C**, **c**) 0.75 conc

photo-sensitivity in visible light, with a band gap of ~3.0 eV. Figure 10c shows the plot of $\ln C_0/C$ of methyl red dye in suspension with irradiation time with all samples. The graph of $\ln C_0/C$ of all samples with respect to irradiation interval is linear, indicating that photocatalytic degradation is first order. The colour of the Methyl Red solution progressively changed from red to light red and then to colourless, which might be seen.

The kinetic study shown as follows [48],

$$\ln(C_0/C) = kt \tag{7}$$

where, C_0 = Initial concentration, C = Final concentration, k = rate constant and t = time. It can be calculated from simulation curve as shown in Fig. 10c. The rate of degradation was monitored by using UV–Visible Spectroscopy and the degradation efficiency was calculated by using formula,

$$\text{Degradation efficiency}(\%) = \frac{C_0 - C}{C_0} \times 100 \tag{8}$$

C_0 and C are the dye concentration at initial and various time.

The $La_{1-x}Al_XY_YFe_{2-Y}O_4$ nano-ferrites catalysed degradation shows 80% degradation efficiency of methyl orange dye.

3.7 Catalyst recyclability

One of the most important features of catalytic efficiency across realistic reuses is the reusability of the produced $La_{1-X}Al_XY_YFe_{2-Y}O_4$ nano-ferrites. As a result, three cycles of photocatalytic methyl red degradation were carried out under sunlight employing $La_{1-X}Al_XY_YFe_{2-Y}O_4$ nano-ferrites, as shown in Fig. 11. After three cycles, the catalyst's exceptional efficiency was revealed, validating the stability of the produced catalysts.

3.8 BET analysis

The surface area and porosity of the $La_{1-X}Al_XY_YFe_{2-Y}O_4$ were measured using the Brunauer Emmett–Teller (BET) equation following the Barrett–Joyner–Halanda method. Figure 12 shows (a) BET surface area and inset, and (b) pore size distribution of $La_{1-X}Al_XY_YFe_{2-Y}O_4$. From the N_2 adsorption–desorption isotherm of $La_{1-X}Al_XY_YFe_{2-Y}O_4$ in Fig. 12, the BET surface area of the particles is 2.688 $m^2\,g^{-1}$. The total pore volume at P/P_0 (0.99) is 5.178 $cm^3\,g^{-1}$. The average pore diameter was found to be 7.704 nm. The isotherm represents type (V), with an H_3 hysteresis loop, which is a characteristic of mesoporous materials.

4 Conclusion

A sol–gel method was used successfully to produce $La_{1-X}Al_XY_YFe_{2-Y}O_4$ nano-ferrites. The structural, magnetic, and optical properties of trivalent yttrium ion in La–Al–Y ferrite nanoparticles were examined. With an optical band gap of 2.9–3.1, the highest absorption occurs at ~265 nm. XRD analysis reveals a cubic spinel closed packed

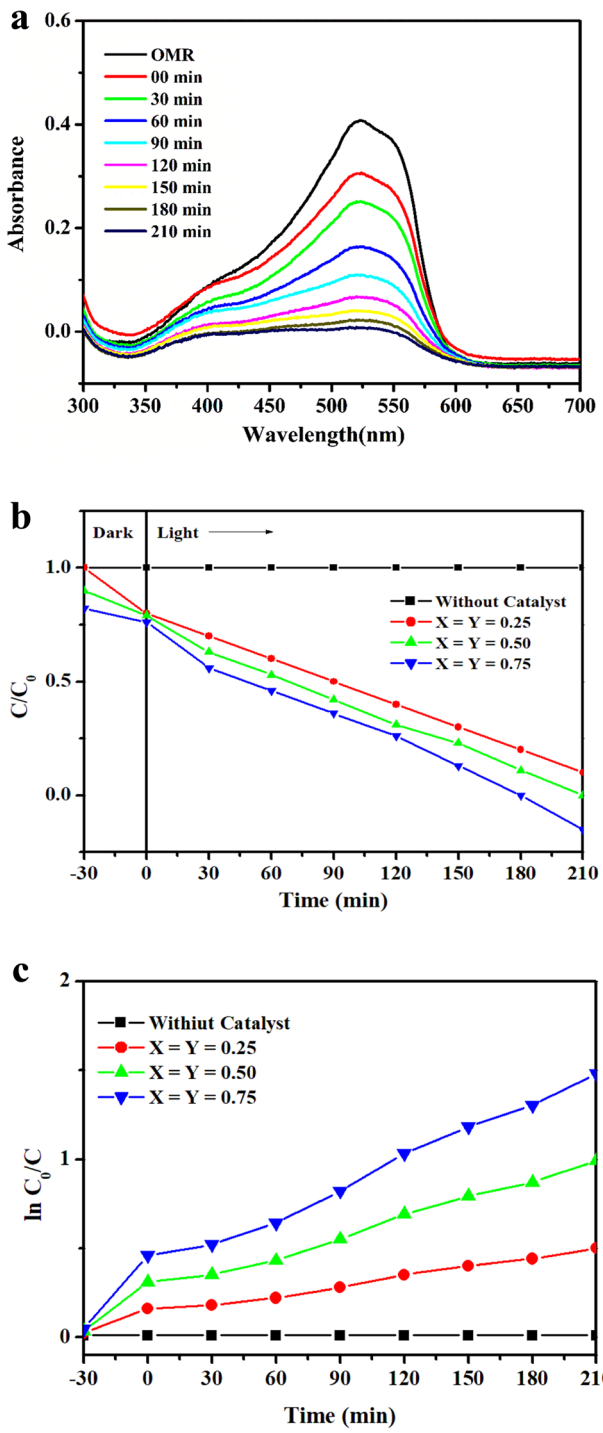

Fig. 10 **a** Optical absorption spectra of methyl red. **b** Kinetic plot of Methyl Red photo degradation reaction. **c** Corresponding plot of ln C_0/C vs time

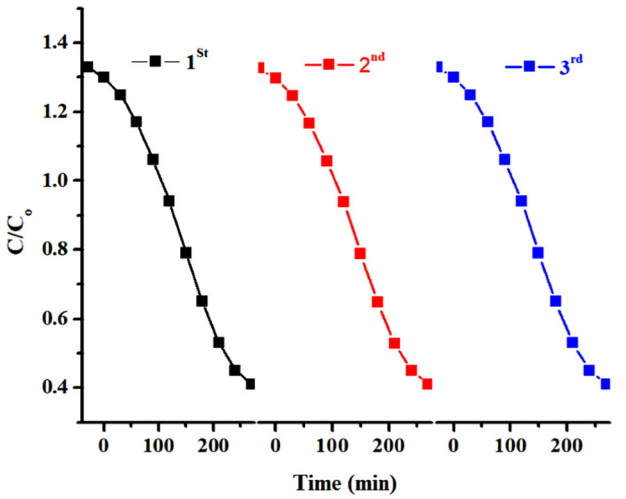

Fig. 11 Catalyst recyclability

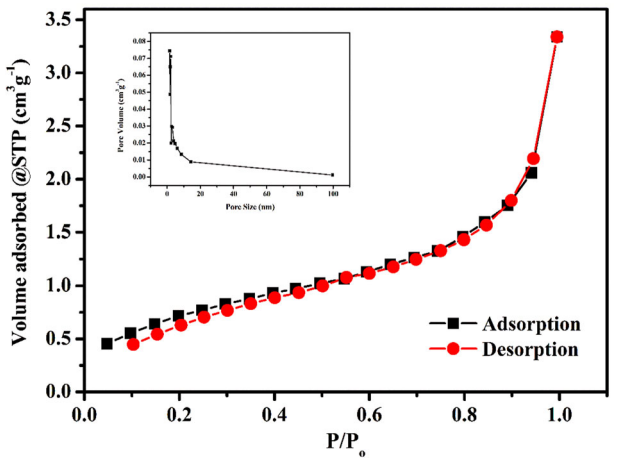

Fig. 12 BET surface area and (Inset) Pore Size distribution of $La_{1-X}Al_XY_YFe_{2-Y}O_4$ nanoferrite

structure (FCC) with no impurity peaks. The crystallite size and particle size were found to be in the 20–30 nm range using the Scherrer formula. The HR-TEM show the particle size and 80–110 nm and confirms the crystalline nature of prepared nano-ferrites. The composition purity was validated using EDS analysis. Because lanthanum, aluminium, and yttrium are paramagnetic magnetic materials, the addition of Al^{3+}, and Y^{3+} influence on M_S. Their Bohr magneton enhanced as the anisotropic constant value increases. From BET analysis, the surface area, pore volume and pore diameter are 2.688 $m^2\ g^{-1}$, 5.178 $cm^3\ g^{-1}$ and 7.704 nm, respectively. This study reveals the nanoparticles are in mesoporous form.The isotherm represents type (V), with an H_3 hysteresis loop. The $La_{1-X}Al_XY_YFe_{2-Y}O_4$nano-ferrites shows the excellent photoactive material and used for the degradation of methyl red dye within 210 min successfully.

Acknowledgements We are obliged to Dr. Babasaheb Ambedkar Marathwada University Sub – Campus Osmanabad for carrying out this research work and UGC New Delhi for providing financial assistance under Maulana Azad National Fellowship to SKK (F1-17.1/2014-15/MANF-2014-15-MUS-MAH-47640/SA-III/Website).

Compliance with ethical standards

Conflict of interest The authors declare no competing interests.

References

1. Bloesser A, Kurz H, Timm J, Wittkamp F, Simon C, Hayama S, Weber B, Apfel U-P, Marschall R (2020) Tailoring the size, inversion parameter, and absorption of phase-pure magnetic $MgFe_2O_4$ nanoparticles for photocatalytic degradations. ACS Appl Nano Mater 3(11):11587–11599. https://doi.org/10.1021/acsanm.0c02705
2. Ebrahimi M, Akhavan O (2022) Nanomaterials for photocatalytic degradations of analgesic, mucolytic and anti-biotic/viral/inflammatory drugs widely used in controlling SARS-CoV-2. Catalysts 12(6). https://doi.org/10.3390/catal12060667
3. Tiano AL, Papaefthymiou GC, Lewis CS, Han J, Zhang C, Li Q, Shi C, Abeykoon AMM, Billinge SJL, Stach E, Thomas J, Guerrero K, Munayco P, Munayco J, Scorzelli RB, Burnham P, Viescas AJ, Wong SS (2015) Correlating size and composition-dependent effects with magnetic, Mössbauer, and pair distribution function measurements in a family of catalytically active ferrite nanoparticles. Chem Mater 27(10):3572–3592. https://doi.org/10.1021/acs.chemmater.5b00767
4. González-Calbet JM, Parras M, Vallet-Regí M, Grenier JC (1991) Anionic vacancy distribution in reduced barium-lanthanum ferrites: $Ba_xLa_{1-x}FeO_{3-x}2$ (12 ≤ x ≤ 23). J Solid State Chem 92(1):110–115. https://doi.org/10.1016/0022-4596(91)90247-F
5. Ten Elshof JE, Lankhorst MHR, Bouwmeester HJM (1997) Oxygen exchange and diffusion coefficients of strontium-doped lanthanum ferrites by electrical conductivity relaxation. J Electrochem Soc 144(3):1060–1067. https://doi.org/10.1149/1.1837531
6. Coffey GW, Hardy J, Rpedersen L, Crieke P, Thomsen EC, Walpole M (2003) Electrochemical properties of lanthanum strontium aluminumferrites for the oxygen reduction reaction. Solid State Ion 158:1–9
7. Coffey GW, Hardy JS, Pederson LR, Rieke PC, Thomsen EC (2003) Oxygen reduction activity of lanthanum strontium nickel ferrite. Electrochem Solid-State Lett 6(6):A121–A124
8. Mitoseriu L, Buscaglia V, Viviani M, Buscaglia MT, Pallecchi I, Harnagea C, Testino A, Trefiletti V, Nanni P, Siri A (2007) $BaTiO_3$–(Ni0.5Zn0.5)Fe_2O_4 ceramic composites with ferroelectric and magnetic properties. J Eur Ceram Soc 27:4379–4382. https://doi.org/10.1016/j.jeurceramsoc.2007.02.167
9. Mitoseriu L, Pallecchi I, Buscaglia V, Testino A, Stancu A (2007) Magnetic properties of the $BaTiO_3$-(Ni,Zn)Fe_2O_4 multiferroic composites. J Magn Magn Mater 316. https://doi.org/10.1016/j.jmmm.2007.03.036.
10. Zink PA, Yoon KJ, Pal UB, Gopalan S (2009) Analysis of the electronic and ionic conductivity of calcium-doped lanthanum ferrite. Electrochem Solid-State Lett 12(10):B141. https://doi.org/10.1149/1.3182805
11. González-Calbet JM, Vallet-Regi M, Alario-Franco MA, Grenier JC (1983) Structural intergrowths in the calcium lanthanum ferrites: $Ca_xLa_{1-x}FeO_{3-Y}$ (23 < x < 1). Mater Res Bull 18(3):285–292. https://doi.org/10.1016/0025-5408(83)90115-0
12. Alario-Franco MA, Gonzalez-Calbet JM, Vallet-Regi M, Grenier JC (1983) Brownmillerite-type microdomains in the calcium lanthanum ferrites: $Ca_xLa_{1-x}FeO_{3-y}$: I. 23 < x < 1. J Solid State Chem 49(2):219–231. https://doi.org/10.1016/0022-4596(83)90116-0
13. Natali Sora I, Caronna T, Fontana F, de Julián Fernández C, Caneschi A, Green M (2012) Crystal structures and magnetic properties of strontium and copper doped lanthanum ferrites. J Solid State Chem 191:33–39. https://doi.org/10.1016/j.jssc.2012.02.020
14. Nesa F, Zakaria AKM, Khan MAS, Yunus SM, Das AK, Eriksson S-G, Khan MNI, Hakim MA (2012) Structural and magnetic properties of Cr^{3+};doped Mg ferrites. World J Condens Matter Phys 2:9. https://doi.org/10.4236/wjcmp.2012.21005
15. Onreabroy W, Papato K, Rujijanagul G, Pengpat K, Tunkasiri T (2012) Study of strontium ferrites substituted by lanthanum on the structural and magnetic properties. Ceram Int 38:S415–S419. https://doi.org/10.1016/j.ceramint.2011.05.023
16. Stergiou C, Litsardakis G (2014) Structural and magnetic properties of yttrium and lanthanum-doped Ni-Co and Ni-Co-Zn spinel ferrites. AIP Conf Proc 1627(1):117–122. https://doi.org/10.1063/1.4901668
17. Rai A, Sharma AL, Thakur AK (2014) Evaluation of aluminium doped lanthanum ferrite based electrodes for supercapacitor design. Solid State Ion 262:230–233. https://doi.org/10.1016/j.ssi.2013.10.024
18. Kuznetsov MV, Morozov IG, Parkin IP (2015) Self-propagating high-temperature synthesis of aluminum substituted lanthanum ferrites $LaFe_{1-x}Al_xO_3$ (0 ≤ x ≤ 1.0). N J Chem 39(12):9834–9840. https://doi.org/10.1039/c5nj00981b
19. Mazumdar SC, Khan MNI, Islam MF, Hossain AKMA (2015) Enhanced multiferroic properties in (1–y)$BiFeO_{3-y}Ni_{0.50}$ $Cu_{0.05}Zn_{0.45}Fe_2O_4$ composites. J Magn Magn Mater 390:61–69. https://doi.org/10.1016/j.jmmm.2015.04.087
20. Zhang M, Zi Z, Liu Q, Zhang P, Tang X, Yang J, Zhu X, Sun Y, Dai J(2013) Size effects on magnetic properties prepared by sol-gel method. Adv Mater Sci Eng 2013:609819. https://doi.org/10.1155/2013/609819
21. Beausoleil Ii GL, Price P, Thomsen D, Punnoose A, Ubic R, Misture S, Butt DP (2014) Thermal expansion of alkaline-doped lanthanum ferrite near the Néel temperature. J Am Ceram Soc 97(1):228–234. https://doi.org/10.1111/jace.12625
22. Jauhar S, Singhal S (2014) Chromium and copper substituted lanthanum nano-ferrites: their synthesis, characterization and application studies. J Mol Struct 1075:534–541. https://doi.org/10.1016/j.molstruc.2014.07.022
23. Yun D, Joo JH, Yu J, Yoon HC, Kim J-N, Yoo C-Y (2015) Electrochemical ammonia synthesis from steam and nitrogen using proton conducting yttrium doped barium zirconate electrolyte with silver, platinum, and lanthanum strontium cobalt ferrite electrocatalyst. J Power Sources 284. https://doi.org/10.1016/j.jpowsour.2015.03.002
24. Zurlo F, Natali Sora I, Felice V, Luisetto I, D'Ottavi C, Licoccia S, Di Bartolomeo E (2016) Copper-doped lanthanum ferrites for symmetric SOFCs. Acta Mater 112:77–83. https://doi.org/10.1016/j.actamat.2016.04.015
25. Mazumdar SC, Khan MNI, Islam MF, Hossain AKMA (2016) Tuning of magnetoelectric coupling in (1−y) Bi0.8Dy0.2FeO_3–yNi0.5Zn0.5Fe2O4 multiferroic composites. J Magn Magn Mater 401:443–454. https://doi.org/10.1016/j.jmmm.2015.10.051
26. Choi J, Chung YH (2016) Preparation of lanthanum oxide and lanthanum oxycarbonate layers on titanium by electrodeposition with organic solution. J Nanomaterials 2016:5140219. https://doi.org/10.1155/2016/5140219
27. Aziz HS, Rasheed S, Khan RA, Rahim A, Nisar J, Shah SM, Iqbal F, Khan AR (2016) Evaluation of electrical, dielectric and magnetic characteristics of Al–La doped nickel spinel ferrites. RSC Adv 6(8):6589–6597. https://doi.org/10.1039/c5ra20981a

28. Bhujun B, Tan M, Shanmugam S (2016) Evaluation of aluminium doped spinel ferrite electrodes for supercapacitors. Ceram Int 42. https://doi.org/10.1016/j.ceramint.2015.12.118
29. Kanna RR, Nayagam L, Kathiresan S, Sivabhabharathy M (2017) Impact of Lanthanum on structural, optical, dielectric and magnetic properties of $Mn_{1-x}Cu_xFe_{1.85}La_{0.15}O_4$ spinel nanoferrites. Ceram Int 43. https://doi.org/10.1016/j.ceramint.2017.08.160
30. Ali MA, Uddin MM, Khan MNI, Chowdhury FUZ, Haque SM (2017) Structural, morphological and electrical properties of Sn-substituted Ni-Zn ferrites synthesized by double sintering technique. J Magn Magn Mater 424:148–154. https://doi.org/10.1016/j.jmmm.2016.10.027
31. Ullah AKMA, Kibria AKMF, Akter M, Khan MNI, Maksud MA, Jahan RA, Firoz SH (2017) Synthesis of Mn3O4 nanoparticles via a facile gel formation route and study of their phase and structural transformation with distinct surface morphology upon heat treatment. J Saudi Chem Soc 21(7):830–836. https://doi.org/10.1016/j.jscs.2017.03.008
32. Ni C, Cassidy M, Irvine JTS (2018) Image analysis of the porous yttria-stabilized zirconia (YSZ) structure for a lanthanum ferrite-impregnated solid oxide fuel cell (SOFC) electrode. J Eur Ceram Soc 38(16):5463–5470. https://doi.org/10.1016/j.jeurceramsoc.2018.08.026
33. Akhavan O, Meidanchi A, Ghaderi E, Khoei S (2014) Zinc ferrite spinel-graphene in magneto-photothermal therapy of cancer. J Mater Chem B 2(21):3306–3314. https://doi.org/10.1039/c3tb21834a
34. Hajipour MJ, Akhavan O, Meidanchi A, Laurent S, Mahmoudi M (2014) Hyperthermia-induced protein corona improves the therapeutic effects of zinc ferrite spinel-graphene sheets against cancer. RSC Adv 4(107):62557–62565. https://doi.org/10.1039/c4ra10862k
35. Meidanchi A, Akhavan O, Khoei S, Shokri AA, Hajikarimi Z, Khansari N (2015) $ZnFe_2O_4$ nanoparticles as radiosensitizers in radiotherapy of human prostate cancer cells. Mater Sci Eng: C 46:394–399. https://doi.org/10.1016/j.msec.2014.10.062
36. Marcucci A, Luisetto I, Zurlo F, Licoccia S, Di Bartolomeo E (2020) Pd-doped perovskite-based SOFC anodes for biogas. J Solid State Electrochem 24(1):93–100. https://doi.org/10.1007/s10008-019-04473-5
37. Balinski A, Kelly N, Helbig T, Meskers C, Reuter MA (2020) Separation of aluminum and iron from lanthanum—a comparative study of solvent extraction and hydrolysis-precipitation. Minerals 10(6). https://doi.org/10.3390/min10060556
38. Hossen MM, Hossen MB (2020) Structural, electrical and magnetic properties of Ni0.5Cu0.2Cd0.3LaxFe2-xO4 nano-ferrites due to lanthanum doping in the place of trivalent iron. Phys B: Condens Matter 585:412116. https://doi.org/10.1016/j.physb.2020.412116
39. Yousuf MA, Jabeen S, Shahi MN, Khan MA, Shakir I, Warsi MF (2020) Magnetic and electrical properties of yttrium substituted manganese ferrite nanoparticles prepared via micro-emulsion route. Results Phys 16:102973. https://doi.org/10.1016/j.rinp.2020.102973
40. Nilmoung S, Khajonrit J, Sonsupap S, Maensiri S (2020) Activated carbon nanofibers/aluminium doped-copper manganese ferrite composite nanostructures for electrochemical capacitors. J Energy Storage 31:101777. https://doi.org/10.1016/j.est.2020.101777
41. Shahzadi K, Chandio AD, Mustafa G, Khalid M, Khan JK, Akhtar MS, Gilani ZA, Asgar HMNuHK (2020) Impact of aluminum substitution on the structural and dielectric properties of Ni–Cu spinel ferrite nanoparticles synthesized via sol–gel route. Optical Quantum Electron 52(4):190. https://doi.org/10.1007/s11082-020-02304-w
42. Ur. rehman A, Ashraf MW, Tayyaba S, Bashir M, Wasim MF, Imran M (2021) Synthesis and growth of bismuth ferrite (BiFeO3) with Lanthanum (la) and Yttrium(y) doped nano-structures on anodic aluminum oxide (AAO) template. Dig J Nanomater Biostruct 16(1):231–238
43. Sankaranarayanan R, Shailajha S, Mubina MS, Anilkumar CP (2021) Influence of divalent ions on structural, magnetic and electrical response of $Co_zCd_yZn_xNi_{(1-x-y-z)}Fe_2O_4$ core materials. J Magn Magn Mater 529:167892. https://doi.org/10.1016/j.jmmm.2021.167892
44. Price PM, Butt DP (2015) Stability and decomposition of Ca-substituted lanthanum ferrite in reducing atmospheres. J Am Ceram Soc 98(9):2881–2886. https://doi.org/10.1111/jace.13569
45. Casey KC, Brown AM, Robinson JR (2021) Yttrium and lanthanum bis(phosphine-oxide)methanides: structurally diverse, dynamic, and reactive. Inorg Chem Front 8(6):1539–1552. https://doi.org/10.1039/d0qi01438a
46. Parras M, Vallet-Regi M, Gonza´lez-Calbet JM, Alario-Franco M, Grenier JC (1988) Electron microscopy and diffraction of barium-lanthanum ferrites: $Ba_xLa_{1-x}FeO_{3-y}$. J Solid State Chem 74(1):110–116. https://doi.org/10.1016/0022-4596(88)90336-2
47. Chiwandika EK, Cho S-K, Jung S-M (2020) Phase development in the sintering of a hematite–ilmenite ore blend. Minerals 10(9). https://doi.org/10.3390/min10090800.
48. Muhammad Y, Hamdani U, Puji W, Rachmad Almi P (2019) Characterization of microstructural and optical $CoFe_2O_4/SiO_2$ ferrite nanocomposite for photodegradation of methylene blue. AIMS Mater Sci 6(1):45–51. https://doi.org/10.3934/matersci.2019.1.45
49. Kazi SK, Inamdar SN, Kamble DP, Lohar KS, Suryawanshi AW, Tigote RM (2022) Structural studies of silica-supported spinel magnesium ferrite nanorods for photocatalytic degradation of methyl orange. J Chin Chem Soc 69(7):1032–1041. https://doi.org/10.1002/jccs.202200010
50. Wang L, Li J, Wang Y, Zhao L, Jiang Q (2012) Adsorption capability for Congo red on nanocrystalline MFe_2O_4 (M=Mn, Fe, Co, Ni) spinel ferrites. Chem Eng J 181-182:72–79. https://doi.org/10.1016/j.cej.2011.10.088
51. Meidanchi A, Akhavan O (2014) Superparamagnetic zinc ferrite spinel–graphene nanostructures for fast wastewater purification. Carbon 69:230–238. https://doi.org/10.1016/j.carbon.2013.12.019